



ALMA MATER STUDIORUM
UNIVERSITÀ DI BOLOGNA

ARCHIVIO ISTITUZIONALE
DELLA RICERCA

Alma Mater Studiorum Università di Bologna Archivio istituzionale della ricerca

Multistatic Parameter Estimation in the Near/Far Field for Integrated Sensing and Communication

This is the final peer-reviewed author's accepted manuscript (postprint) of the following publication:

Published Version:

Dehkordi, S.K., Pucci, L., Jung, P., Giorgetti, A., Paolini, E., Caire, G. (2024). Multistatic Parameter Estimation in the Near/Far Field for Integrated Sensing and Communication. IEEE TRANSACTIONS ON WIRELESS COMMUNICATIONS, 23(12), 17929-17944 [10.1109/twc.2024.3458048].

Availability:

This version is available at: <https://hdl.handle.net/11585/1003168> since: 2025-01-27

Published:

DOI: <http://doi.org/10.1109/twc.2024.3458048>

Terms of use:

Some rights reserved. The terms and conditions for the reuse of this version of the manuscript are specified in the publishing policy. For all terms of use and more information see the publisher's website.

This item was downloaded from IRIS Università di Bologna (<https://cris.unibo.it/>).
When citing, please refer to the published version.

(Article begins on next page)

Multistatic Parameter Estimation in the Near/Far Field for Integrated Sensing and Communication

Saeid K. Dehkordi, Lorenzo Pucci, Peter Jung, Andrea Giorgetti, Enrico Paolini, Giuseppe Caire

Abstract—This work proposes a maximum likelihood (ML)-based parameter estimation framework for a millimeter wave (mmWave) integrated sensing and communication (ISAC) system in a multistatic configuration using energy-efficient hybrid digital-analog (HDA) arrays. Due to the typically large arrays deployed in the higher frequency bands to mitigate isotropic path loss, such arrays may operate in the near-field (NF) regime. The proposed parameter estimation in this work consists of a two-stage estimation process, where the first stage is based on far-field (FF) assumptions, and is used to obtain a first estimate of the target parameters. In cases where the target is determined to be in the NF of the arrays, a second estimation based on NF assumptions is carried out to obtain more accurate estimates. In particular, when operating in the near-field of the transmitter (Tx), we select *beamfocusing* array weights designed to achieve a constant gain over an extended spatial region and re-estimate the target parameters at the receivers (Rxs). We evaluate the effectiveness of the proposed framework in numerous scenarios through numerical simulations and demonstrate the impact of the custom-designed flat-gain beamfocusing codewords in increasing the communication performance of the system.

Index Terms—integrated sensing and communication, OFDM, near-field parameter estimation, multistatic ISAC.

I. INTRODUCTION

In the context of 5G and beyond wireless systems, integrated sensing and communication (ISAC) has emerged as one of the key components [1]. Unlike active localization in existing mobile systems, where the user equipments (UEs) interact with the base stations (BSs) for position estimation, ISAC systems enable a wireless network to localize passive objects in the environment. By collecting and analyzing the signals reflected from these objects, ISAC systems use the same hardware and physical layer resources for both communication and sensing, leading to more efficient spectrum utilization. Integrating sensing into next-generation mobile systems unlocks new capabilities for applications like traffic monitoring, pedestrian detection, and urban autonomous driving [2]. Recent studies have demonstrated the potential of employing orthogonal

frequency division multiplexing (OFDM)-based waveforms for ISAC systems, with a focus in particular on the monostatic configuration, that is, with the transmitter (Tx) and receiver (Rx) co-located [3], [4], [5], [6]. However, this configuration requires additional hardware or digital processing to remove self-interference [4].

A possible solution to avoid the self-interference problem is to use a bistatic configuration, where the Tx and Rx are not co-located. Bistatic radar setups are also beneficial for extending the sensing coverage area using cost-effective Rx units, which can also be mobile [7]. For these reasons, bistatic and multistatic ISAC configurations are attracting increasing amounts of interest for future 5th generation and beyond (5G) networks [8], [9]. In order to achieve the required level of delay and angle resolution, radar sensing requires large antenna arrays and wideband signals. Communication waveforms (such as OFDM) in 5G are expected to use high frequencies (28 — 100 GHz) and large signal bandwidths. Due to the small wavelength, large arrays can be implemented in relatively small form factors. However, the implementation of fully digital architectures becomes extremely challenging due to the enormous data rate of the A/D conversion at each antenna element. In order to alleviate this problem, hybrid digital-analog (HDA) architectures are commonly considered for massive multiple-input multiple-output (MIMO) communications. Another interesting aspect connected to the use of very large arrays is that, for some users and radar targets, the usual far-field (FF) assumption common to most array processing literature is not satisfied any longer [10]. In the case of near-field (NF) propagation, the usual modeling of the received signal as a superposition of planar waves impinging on the array from multiple scattering elements is not valid, and NF-specific algorithm design for communication and sensing is required.

While most of the available literature focuses on the two extreme cases (either the FF or NF regime [11]) for the algorithmic design of ISAC systems, to the best of the authors' knowledge, the state-of-the-art still lacks studies on the sensing and communication performance of a multistatic (or bistatic) ISAC system, taking into account both NF and FF scenarios. In order to employ a beamforming/beamfocusing scheme adapted to the propagation scenario, it is necessary to determine whether the radar target (or the UE) is in FF or NF conditions. This requires some initial estimation, that is agnostic of the propagation conditions. For this reason, this work considers a multistatic ISAC configuration composed of two bistatic pairs, capable of detecting and localizing extended sensing objects that are located in the NF or FF of the Tx and/or one of

The authors would like to acknowledge the financial support by the Federal Ministry of Education and Research of Germany in the program of "Souverän. Digital. Vernetzt." Joint project 6G-RIC, project identification number: 16KISK030, and by the European Union under the Italian National Recovery and Resilience Plan (NRRP) of NextGenerationEU, partnership on "Telecommunications of the Future" (PE00000001 - program "RESTART").

S. K. Dehkordi and G. Caire are with the Technical University of Berlin, Germany (e-mail: {s.khalilidehkordi, caire}@tu-berlin.de). P. Jung is with the Technical University of Berlin and the German Aerospace Center (DLR), Germany (e-mail: peter.jung@tu-berlin.de).

L. Pucci, A. Giorgetti, and E. Paolini are with CNIT/WiLab and the Department of Electrical, Electronic, and Information Engineering "Guglielmo Marconi" University of Bologna, Italy (e-mail: {lorenzo.pucci3 andrea.giorgetti, e.paolini}@unibo.it).

the Rx without a priori knowledge. Moreover, unlike several works on ISAC where the integrated sensing signal is used to detect and localize passive objects not directly connected to the network, this work considers a scenario where targets are UEs and where sensing can be used to improve communication performance. As will be explained later, in this case, instead of reserving a portion of the physical layer resources (i.e., frequency band, time, and/or power) for sensing, the same data-carrying downlink signal sent by the Tx to communicate with the UEs can be used as a sensing signal by collecting the scattered signals at the (sensing) Rxs.

Motivated by the lower dimensionality of the beamforming codebook and the reduced parameter search space of the FF model, the proposed framework *initializes* the sensing operation in the beam space by using FF beamforming vectors and performing maximum likelihood (ML) detection and estimation. Based on the target estimation obtained from this initial stage of sensing, the strategy for the second stage is determined. If the target is detected to be in FF of both the Tx and Rx arrays, a second stage is not required. Nevertheless, as shown in our previous work [5], with adequately accurate positional estimates, it is possible to switch to FF beamformers with higher directivity to increase the operating signal-to-noise ratio (SNR). If the target is determined to be in the NF of an Rx array, the second stage performs another ML estimation of the target parameters using the correct NF model, since the FF model used in the first stage is mismatched. This adjustment leads to significantly improved estimation performance. If the presence of targets in the NF of the Tx is detected, the scheme switches the Tx beamforming to a beamfocusing approach, thus increasing the SNR at the intended target location.

In the communication-only context, which requires some active scheme between the BS and UE, two-step beamformer/beamfocuser design procedures have also been advocated in other works (e.g., [12], [13]). It should be noted that in the considered scenario, where the detected target is a communication user, the ability to properly illuminate it can lead to a significant increase in communication performance, such as improved spectral efficiency.

To obtain the beamfocusing weights, a beamfocusing codebook at the Tx is employed, where the codewords are designed to maintain a nearly constant gain within an extended spatial region. Recently, there has been significant research on NF beamfocusing schemes, particularly in the reconfigurable reflecting surfaces domain, due to the large array sizes used therein [14], [15]. While a few studies have investigated using beamfocusing weights derived by conjugating the NF array response, others have resorted to optimization-based methods to obtain suitable weights [16], [10]. The most significant drawback of those methods is that a very accurate estimate of the intended user coordinates (equivalently *range* and *angle*) is required (see (4) for the array response). Even when ignoring the cost of obtaining such estimates, these techniques pose another significant challenge since the goal is to focus beams on the UE's antenna. However, in the very likely scenario of physically extended targets (ETs) (e.g., motorbikes, bicycles, cars, etc.) the UE antenna can be located anywhere on the object and the estimated reflection points do not necessarily

correspond to the reflections from the antenna. In other works, NF codebook-based techniques have been employed. Some of the more promising approaches are the *Ring-type Codebook* designs [15], where a first layer phase distribution is calculated based on the Fresnel principle and is then superimposed with the codeword selected from a (FF) discrete Fourier transform (DFT) codebook in the second layer. As shown in [15], such designs can lead to significant spectral leakages in unwanted locations, which undermines the goal of user-interference reduction via beamfocusing. From the sensing perspective, this leads to reflection from unintended objects that may be located in the undesired illuminated areas.

To address these issues, we present a method that aims to synthesize beamfocusing weights for array operation in the NF such that an extended area, centered at specific (range, angle) coordinates, is illuminated with a relatively constant gain. This method is inspired by flat-top beamforming techniques, which aim to provide an (almost-) constant gain over an extended angular span (see, e.g., [5] and references therein for details), and are considered in this work for FF beamforming operations. In accordance with [17], [13], our numerical results show that the beamfocusing scheme converges to beamforming within the transitional region between the NF and FF.

Given all these points, this work proposes a unified multistatic ISAC model that addresses the estimation of target parameters in both NF and FF regions, within a typical urban scenario, using HDA architectures. The main contributions are highlighted as follows:

- 1) We introduce a general sensing channel model for OFDM-based multistatic ISAC systems that is valid for both NF and FF conditions. This model accounts for amplitude and phase variations at different antenna elements in the NF and converges to the well-known line-of-sight (LoS) propagation model in the FF. We then propose a two-stage estimation procedure to estimate target parameters without prior knowledge of whether the target is in the NF or FF of the multistatic deployment topology. Initially, a rough estimate is obtained under the assumption of FF conditions, which is refined using the correct NF model if necessary. This approach contrasts with the existing studies on ISAC, which typically assume prior knowledge of operating exclusively in either the NF or FF.
- 2) Recognizing that real-world objects, like cars, are unlikely to produce single reflections and instead appear as ETs, especially when large bandwidths are considered, we introduce a model to represent targets as extended objects composed of multiple scattering points. This model consists of a grid where each point can be active or inactive during radar measurement, following a binomial distribution. We demonstrate through numerical results that fusing information from two Rxs significantly increases target detection performance. This improvement is attributed to the multistatic radar configuration, which allows viewing ETs from different perspectives, thus generating a diversity gain.
- 3) Inspired by flat-top beamforming techniques [5], we introduce an optimization technique to obtain beamfo-

cusing codewords designed to illuminate a large region of space with an approximately constant gain. This approach allows proper illumination of extended objects and overcomes the target illumination problems that can arise in the NF when using beamfocusing methods based on complex conjugate array responses. We then demonstrate that it is possible to drastically improve localization and communication performance by using beamfocusing instead of beamforming when the target (or UE) is determined to be in the NF of the Tx.

- 4) Extending the approach presented in [5] to the NF case, we propose a beam-space processing method for angle of arrival (AoA) estimation with HDA architectures in both NF and FF. This method is fully compliant with the considered codebook-based scheme.

We adopt the following notations: capital boldface letters for matrices, lowercase bold letters for vectors, $(\cdot)^*$ and $(\cdot)^T$ denote the complex conjugate and transpose operations, respectively, while $(\cdot)^H$ denotes the Hermitian (conjugate and transpose) operation. $|x|$ denotes the absolute value of x if $x \in \mathbb{R}$, while $|\mathcal{X}|$ denotes the cardinality of a set \mathcal{X} . $\|\mathbf{x}\|_2$ denotes the ℓ_2 -norm of a complex or real vector \mathbf{x} . A zero-mean circularly symmetric complex Gaussian random vector with covariance $\mathbf{\Sigma}$ is denoted by $\mathbf{x} \sim \mathcal{CN}(\mathbf{0}, \mathbf{\Sigma})$. \mathbf{I}_m denotes the $m \times m$ identity matrix. We let $[n] = \{1, \dots, n\}$ and $[0 : n] = \{0, 1, \dots, n\}$ for a positive integer n . \otimes denotes the Kronecker product.

The rest of the paper is organized as follows. In Section II, the considered ET model, the NF/FF regions relationship, and the generalized NF/FF sensing channel model are given, while Section III provides the OFDM input-output relationship for a single bistatic system in the presence of reflections from ETs. In Section IV, the ML estimator is derived and our two-stage parameter estimation framework is presented. Section V introduces a novel algorithm that generates a beamfocusing codebook, ensuring a constant gain across an extended spatial area. Numerical results are presented in Section VI, and Section VII concludes the paper with some remarks.

II. SYSTEM MODEL

In this paper, a multistatic ISAC configuration is considered. In particular, as shown in Fig. 3, the system consists of a Tx and two Rx units to form two bistatic Tx-Rx pairs. By using multiple Rxs, it is possible to see the targets from different perspectives, thus providing a diversity gain, especially in the case of ETs. In fact, a well-known advantage of bistatic/multistatic sensing configurations is to provide an enhanced radar cross section (RCS) based observation of targets (i.e., compared to the monostatic configuration), since different observation perspectives of targets result in different measurements [18]. Another advantage of bistatic setup is that full-duplex processing, which would otherwise be required for monostatic sensors, is not necessary.¹ As in most of the related literature, we assume that a connection between the Tx and

¹Full-duplex operations can be achieved with sufficient isolation between the Tx and the radar Rx [19], [20], nevertheless are still considered a challenge.

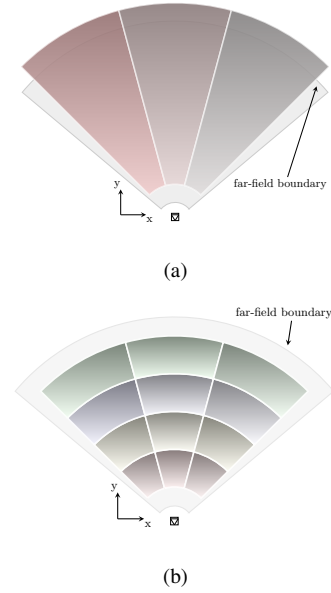


Fig. 1: Schematic representation of a codebook of (a) beamforming and (b) beamfocusing codewords in the spatial domain. Note that the FF beamformers extend beyond the Fraunhofer distance and beamfocusing codewords are designed to (maximally) cover up to the Fraunhofer distance (i.e. the NF region). Refer to IV-B for a discussion on the effective beamfocusing region. Additionally, the codewords do not need to uniformly divide the space. As an example, in typical urban deployments, areas with more densely located users can be assigned more refined codewords and vice versa.

Rx units via either a *wired* backhaul or wireless radio link is established.

In our analysis, we consider OFDM as the modulation scheme since it is widely recognized as one of the standardized waveforms for 5G-NR millimeter wave (mmWave) systems and ISAC applications [21], [22].² Moreover, as mentioned in Section I, the targets considered in this work are UEs. To accomplish both communication and sensing tasks, we consider that the Tx transmits a data-carrying (downlink) frame consisting of N OFDM symbols, for a duration equal to NT_0 and bandwidth of $W = M\Delta f$, where $T_0 = 1/\Delta f + T_{cp}$ is the total OFDM symbol duration including the cyclic prefix, M is the total number of subcarriers, and Δf is the subcarrier spacing. The system operates over a channel with carrier frequency $f_c \gg W$, such that the narrowband array response assumption holds [23]. The generic subcarrier has the frequency $f_m = f_c + m\Delta f$, where $m = -M/2, \dots, M/2 - 1$. Aiming at hardware cost and energy efficiency, we consider a *fully-connected* HDA array architecture (see, e.g., [24]) where the BS at the Tx is equipped with N_{tx}^{rf} Tx radio frequency (RF) chains driving an antenna array with N_{tx} elements. The radar Rxs have the same architecture as the Tx unit, with N_{rx} antenna elements and N_{rx}^{rf} RF chains.

For communication, the BS transmits $1 \leq Q \leq N_{tx}^{rf}$ data streams through a beamforming matrix $\mathbf{F} = [\mathbf{f}_1, \dots, \mathbf{f}_Q]$, where \mathbf{f}_q denotes the q -th column of \mathbf{F} associated to the q -

²Note that the analysis performed is general and remains valid even if a different multi-carrier modulation scheme is chosen, such as orthogonal time frequency space (OTFS).

th data stream. The design of Tx beamformers \mathbf{f}_q involves ensuring that each one covers a relatively wide section of the beam space with a constant gain while maintaining a very low gain elsewhere (see [5] for detailed information). In particular, the Tx beamforming vectors are such that $\mathbf{f}_q^H \mathbf{f}_{q'} \approx 0$, for all $q' \neq q$. Subsequently, the backscattered signals originating from the targets (UEs) within the beam space segments covered by the respective Tx beamforming vectors are utilized for radar processing.

In this work, we assume that the number of legitimate targets (i.e., users) is known via communication between the UEs and the BS, here serving as the host radar. In this context, the beamforming codewords are selected such that each codeword only covers a single target in the beam space. Therefore, we focus on a scenario where a single data stream (i.e., $\mathbf{F} = \mathbf{f}$) is directed towards the UE within a specific sector.

Remark 1. In this study, in addition to the beamforming codebook used for FF beamforming, the second stage of the scheme comprises *beamfocusing* codewords for transmission in the NF. The above assumptions of separated ETs in the FF beam space will also hold in the NF case, where the Tx beamfocusing codewords are designed to be non-overlapping and illuminate only a single ET.

The mmWave systems considered for 5G NR and beyond communications are expected to operate under *codebook*-based schemes (as defined in TS 38.214 [25]). A wide variety of codebook-based schemes have been proposed and investigated in literature (see [26], [27] and refs therein). This work focuses on the estimation of the spatial parameters of ETs that are located in a sensing area resembling an urban deployment, as shown in Fig. 3. Given that our approach operates on a codebook basis, we adopt a time division operation mode. In this mode, a beamforming codeword of the Tx is selected and the Rxs scan the portion of the beam space illuminated by the respective Tx beamformer. Consequently, parameter estimation is carried out specifically within this beam space sector. This process continues sequentially until the entire desired beam space region has been covered. The HDA architecture does not allow conventional MIMO radar processing, and a vector observation of the beam space (i.e., multiple samples of the beam space) is required for angle estimation. To address this, we define a codebook containing a set of N_{rx} DFT orthogonal beams as $\mathcal{U}_{\text{DFT}} := (\mathbf{u}_1, \dots, \mathbf{u}_{N_{\text{rx}}}) \in \mathbb{C}^{N_{\text{rx}} \times N_{\text{rx}}}$ selected from the Fourier basis ($\in \mathbb{C}^{N_{\text{rx}} \times N_{\text{rx}}}$), where N_{rx} is the number of antenna array elements. Subsequently, $N_{\text{rx}}^{\text{rf}}$ beams out of the N_{rx} at the Rx units are selected, ensuring coverage of the desired region of interest (RoI) in the beam space (i.e., the region illuminated by the Tx). This selection results in the formation of a reduction matrix $\mathbf{U} \in \mathbb{C}^{N_{\text{rx}} \times N_{\text{rx}}^{\text{rf}}}$. In scenarios where more than $N_{\text{rx}}^{\text{rf}}$ beams are required to span the illuminated spatial segment, a multi-block-measurement scheme can be adopted (see [5], [28] for details). Such a scheme can easily be justified as a result of minimal target movement over the interval B OFDM blocks required for signal acquisition, where B is typically small.

Remark 2. The HDA system model in this paper can easily be converted to a fully digital system. In this case, $N_{\text{rx}}^{\text{rf}} = N_{\text{rx}}$

RF chains are used to demodulate and sample all the antennas of the radar Rx, thus allowing fully digital processing.

A. Target model

As mentioned above, the analysis in this paper is performed by considering ETs. Two main reasons motivate this choice: 1) An extended real-world object (e.g., a car) is unlikely to produce a single reflection that appears as a point to the radar system. Instead, it is likely to be seen as a set of scatterers, especially when large bandwidths are considered. 2) Accounting for ETs allows the benefits of diversity gain (i.e., the ability of the considered multistatic system to observe the target from different angular directions) to be studied when evaluating system performance in terms of probability of detection. Therefore, a suitable model for ETs is given below.

It is common practice to represent an ET as a set of fixed point-scatterers. As an alternative approach, it is possible to produce a measurement model (likelihood) in terms of the spatial density of measurements in the intended sensing area. Specifically, motivated by finite element discretization techniques commonly used for RCS characterization [29], in this work, the target is modeled as a set of grid elements \mathcal{P} within a designated rectangular region $\mathbf{A} \subset \mathbb{R}^2$ with an area of $|\mathbf{A}|$, as shown in Fig. 2. At each instant the radar measurement is made, the ET representing a UE (e.g., vehicle, motorcycle, etc.) is composed of a random number $P \leq |\mathcal{P}|$ of scatterers. Given that each grid point inside \mathbf{A} can be active with probability q , the number of active points P follows a binomial distribution (BND), with probability q and number of trials $|\mathcal{P}|$, i.e., $P \sim \text{B}(q, |\mathcal{P}|)$.³ Therefore, P points (elements) are drawn i.i.d. from \mathcal{P} such that $P \subseteq \mathcal{P}$.

In the considered channel model, each scattering point (represented by an element) is characterized solely by its LoS path. This is because mmWave channels experience significant isotropic attenuation, making multipath components much weaker than the LoS and often undetectable, as they typically fall below the noise floor after reflection. This effect is especially pronounced in the scattering channel observed by the radar Rxs (see, e.g., [30], [31]). With an appropriate choice of grid size, the varying number of scatterers in the target area can effectively model the fluctuations and variance of an object's radar reflectivity caused by factors such as target aspect angle, material, and more.

Since, in this work, we consider a multistatic system, the reflection points observed by each Rx unit are generated by a separate BND process at each measurement instance.

B. Near/far field regions relationship

The boundary between the NF and FF regions can be determined by the *Fraunhofer* distance (also known as the Rayleigh distance). For an antenna with a maximum aperture D operating at wavelength λ , the Fraunhofer distance, given by $D_{\text{ff}} = \frac{2D^2}{\lambda}$, represents the minimum distance required to

³Interesting to note that, considering a finite but very large number of elements on the grid, i.e., $|\mathcal{P}| \rightarrow \infty$, each of which is independent active or non-active, the binomial distribution can also be very well approximated by a Poisson distribution, with intensity $\gamma = q|\mathcal{P}|$.

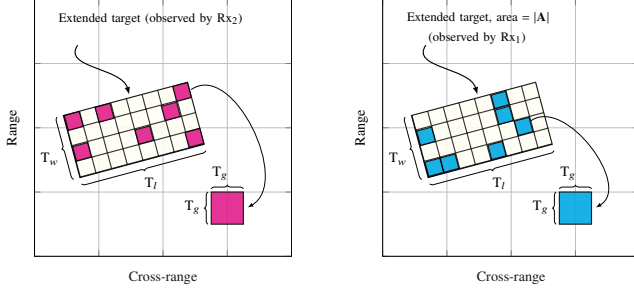


Fig. 2: Schematic of the target model, composed of scattering point clusters determined through a BND. Note that each Rx observes a different scattering profile of the ET at each measurement instance. The parameter values are provided in Tab. II.

ensure that the phase difference of received signals across the array elements is no more than $\pi/8$ [10]. For a uniform linear array (ULA) with N_a elements and $\lambda/2$ inter-element spacing, this equates to $N_a^2\lambda/2$. This is widely considered the limit under which wave propagation under the planar assumption holds. The Fresnel distance D_{fr} , given by $\sqrt{\frac{3D^4}{8\lambda}}$, is the distance beyond which the reactive field components of the antenna become negligible. The distance between D_{ff} and D_{fr} is of interest in this work (see Fig. 3), which is known as the radiative NF Fresnel region, or the NF region for brevity. Note that with multi-band systems, the Fraunhofer distance is impacted by the wavelength of each component [13]. However, for the parameters considered in this paper, the effect of the bandwidth on the Fraunhofer distance is negligible.

Remark 3. The importance of characterizing the boundary between NF and FF regions arises from the inability to illuminate with full array gain through beamforming a target (or UE) that lies in the NF of the antenna array. As will be shown later, in the NF, not a plane but a spherical wavefront should be considered so that the array response depends not only on angle but on both angle and distance (or range). Therefore, a need arises to switch to a beamfocusing approach, where the energy can be focused on a given range-angle region in space. Conversely, using traditional beamforming in the NF results in performance loss in both sensing and communication due to a mismatch in the considered array response [10].

C. Channel model

The considered ISAC system can operate in both NF and FF. In particular, the urban scenario shown in Fig. 3 allows the simultaneous presence of FF and NF conditions in the direct and reflected channels. It is worth noting that a substantial difference between the two regimes can exist in terms of parameter estimation for sensing. In fact, in FF processing, the angle and distance of the target are estimated based on the array response and the time delay of the signal, independently, where the time delay resolution is limited by the system bandwidth. In contrast, in the NF regime, it is possible to directly localize the target without estimating time delay, but only by analyzing the phase of the signal scattered by the target and acquired by different antenna array elements, by exploiting the properties of a spherical wave. However, it is possible to

provide a general formulation of the sensing channel model that is valid for both conditions [13].

For simplicity, we consider for a while a single scatterer p (taken from a generic ET l) located at $\mathbf{p}_p = r_{k,p} [\cos \phi_{k,p}, \sin \phi_{k,p}]^T$ and a transmit ULA k having N_{tx} elements located at $\mathbf{p}_{k_i} = [0, id]^T$, with $i = -\frac{N_{tx}-1}{2}, \dots, \frac{N_{tx}-1}{2}$, the antenna index, and d the spacing between the elements, here set to half the wavelength. We denote $r_{k,p}$ and $\phi_{k,p}$ as the reference distance and reference angle of departure (AoD), respectively, between the Tx k and the scatterer p , calculated with respect to the center of the array. Considering LoS propagation conditions, the equivalent low-pass complex channel coefficient for the channel between the single antenna element i of Tx k and the scatterer p at subcarrier m and time instant n can be written as

$$h_{k_i,p}[m,n] = \sqrt{\xi_{k_i,p}} e^{-j(2\pi(\frac{r_{k_i,p}}{c} f_m - nT_0 v_{k,p}) + \varphi_0)} \quad (1)$$

where $v_{k,p}$ is the reference Doppler shift, $r_{k_i,p} = \|\mathbf{p}_p - \mathbf{p}_{k_i}\|_2$ is the distance between the i -th antenna of Tx k and the scatterer p , c is the speed of light, $\varphi_0 \in \mathcal{U}_{[0,2\pi)}$ is the phase offset between Tx and Rx. Moreover, $\xi_{k_i,p}$ is the gain factor of the channel between the i -th antenna element of Tx k and the scatterer p , which, under LoS conditions, is given by

$$\xi_{k_i,p} = \frac{\sigma_{k,p}}{4\pi r_{k_i,p}^2} \quad (2)$$

with $\sigma_{k,p}$ the RCS of the scatterer p , illuminated by Tx k .

By performing simple algebraic manipulations on (1), the channel vector $\mathbf{h}_{k,p}[m,n] \in \mathbb{C}^{1 \times N_{tx}}$, associated with subcarrier m and scatterer p at time instant n , can be obtained as

$$\mathbf{h}_{k,p}[m,n] = \alpha_{k,p} e^{j2\pi(nT_0 v_{k,p} - m\Delta f \tau_{k,p})} \mathbf{a}^H(\phi_{k,p}, r_{k,p}) \quad (3)$$

where $\alpha_{k,p} = \sqrt{\xi_{k,p}} e^{-j(2\pi f_c \tau_{k,p} + \varphi_0)}$ is the reference channel coefficient associated to the scatterer p and computed with respect to the center of the antenna array; $\tau_{k,p} = r_{k,p}/c$ is the reference propagation delay and $\xi_{k,p}$ the reference channel gain, while $\mathbf{a}(\phi_{k,p}, r_{k,p}) \in \mathbb{C}^{N_{tx} \times 1}$ is the array response vector given by

$$\mathbf{a}(\phi_{k,p}, r_{k,p}) = \begin{pmatrix} \frac{r_{k,p}}{r_{0,p}} \exp\left(-j\frac{2\pi f_c}{c}(r_{0,p} - r_{k,p})\right) \\ \vdots \\ \frac{r_{k,p}}{r_{k_i,p}} \exp\left(-j\frac{2\pi f_c}{c}(r_{k_i,p} - r_{k,p})\right) \\ \vdots \\ \frac{r_{k,p}}{r_{N_{tx}-1,p}} \exp\left(-j\frac{2\pi f_c}{c}(r_{N_{tx}-1,p} - r_{k,p})\right) \end{pmatrix}. \quad (4)$$

It is easy to prove that if FF propagation conditions are taken into account, (4) reduces to [13]

$$\mathbf{a}(\phi_{k,p}) = [e^{-j\frac{2\pi f_c}{c} \frac{N_{tx}-1}{2} d \sin \phi_{k,p}}, \dots, e^{j\frac{2\pi f_c}{c} \frac{N_{tx}-1}{2} d \sin \phi_{k,p}}]^T. \quad (5)$$

Similarly, the vector $\mathbf{h}_{p,j}[m,n] \in \mathbb{C}^{N_{rx} \times 1}$, representing the channel between a given scatterer p and an Rx unit j (which consists of N_{rx} antenna elements) for the m -th subcarrier at a generic time instant n , is given by

$$\mathbf{h}_{p,j}[m,n] = \beta_{p,j} e^{j2\pi(nT_0 v_{p,j} - m\Delta f \tau_{p,j})} \mathbf{b}(\theta_{p,j}, \gamma_{p,j}) \quad (6)$$

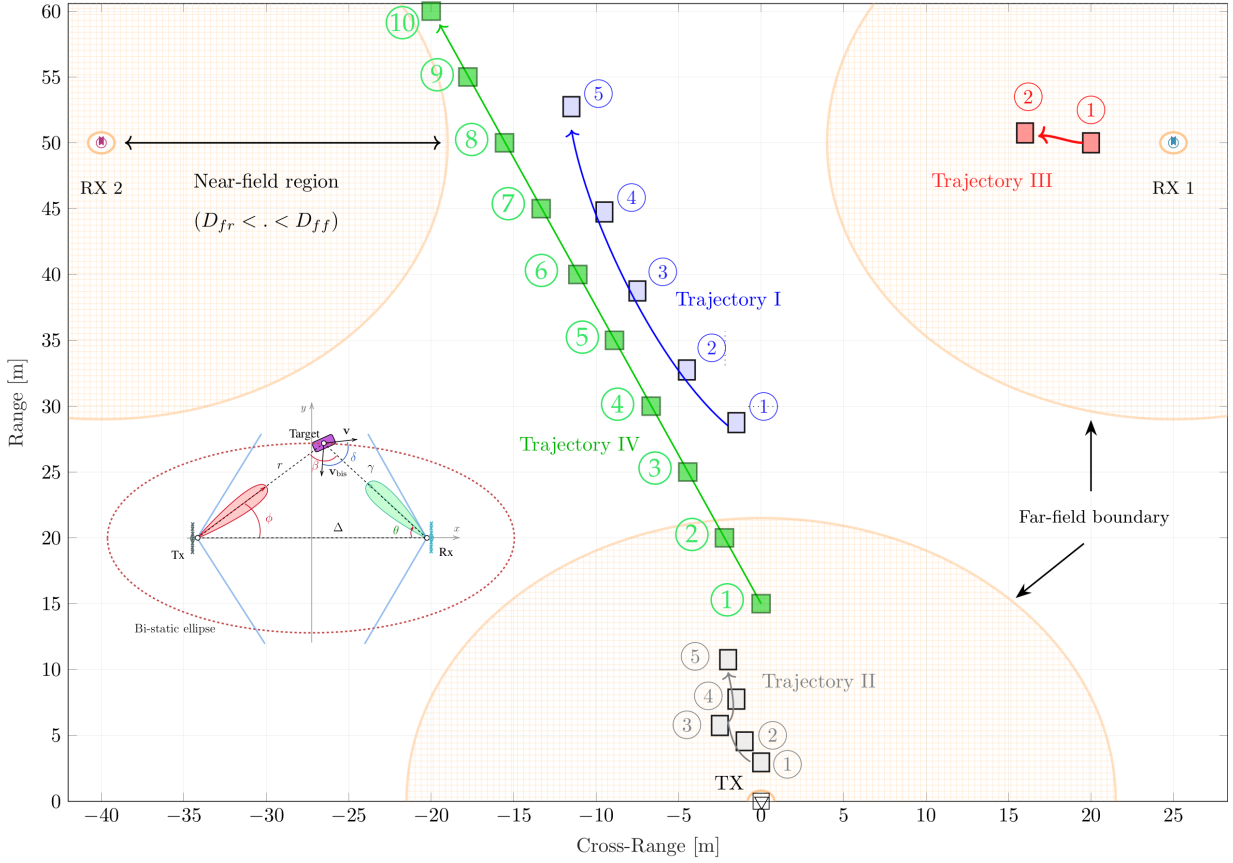


Fig. 3: System topology resembling an urban deployment scenario. The trajectories shown in the figure represent various locations and movement patterns relative to the NF and FF of the antenna arrays. The parameter estimation aspects of each trajectory are investigated separately in Section VI. We assume that the deployment is planned such that the NFs of the Tx/Rx pairs do not overlap. The inset depicts the geometric relation between a Tx/Rx pair and the bistatic ellipse described in Section IV-B.

where $\tau_{p,j} = \gamma_{p,j}/c$ is the reference propagation delay, with $\gamma_{p,j}$ the distance between the scatterer p and the center of the antenna array j , $\beta_{p,j} = \sqrt{\zeta_{p,j}}e^{-j2\pi f_c \tau_{p,j}}$ is the reference channel coefficient, while $\mathbf{b}(\theta_{p,j}, \gamma_{p,j}) \in \mathbb{C}^{N_{\text{rx}} \times 1}$ is the array response vector computed as in (4), being $\theta_{p,j}$ the reference AoA. Considering LoS propagation conditions and isotropic antenna elements with effective area $A = c^2/(4\pi f_c^2)$, the gain factor $\zeta_{p,j}$ can be written as

$$\zeta_{p,j} = \frac{c^2}{(4\pi f_c \gamma_{p,j})^2}. \quad (7)$$

Now, we consider a generic ET l , which is modeled as a group of independent scatterers generated according to a BND, as described in Section II-A. Each of the Tx-Rx bistatic pairs with index (k, j) can collect echoes from a random set $P_{k,j}^{(l)} \subseteq \mathcal{P}$ of these points.⁴ Considering (3) and (6), the $P \times N_{\text{rx}}$ channel between the Tx k and the target l , and the $N_{\text{rx}} \times P$ channel between the Rx j and the target l , at subcarrier m and time instant n can be written as

$$\mathbf{H}_{k,l}[m, n] = \left[\mathbf{h}_{k,1}^{\text{T}}[m, n], \dots, \mathbf{h}_{k,P}^{\text{T}}[m, n] \right]^{\text{T}} \quad (8)$$

⁴In the following, for the sake of brevity, we denote by $P = |P_{k,j}^{(l)}|$ the random number of scatterers related to the target l and seen by the bistatic pair (k, j) .

and

$$\mathbf{H}_{l,j}[m, n] = \left[\mathbf{h}_{1,j}[m, n], \dots, \mathbf{h}_{P,j}[m, n] \right] \quad (9)$$

respectively.

Starting from (8) and (9), the $N_{\text{rx}} \times N_{\text{tx}}$ bistatic MIMO channel between Tx k and Rx j , considering the presence of an ET l , at m -th subcarrier and n -th time slot can be expressed as follows

$$\begin{aligned} \mathbf{H}_{k,j}[m, n] &= \mathbf{H}_{l,j}[m, n] \mathbf{H}_{k,l}[m, n] \\ &= \sum_{p=1}^P \varepsilon_p e^{j2\pi(nT_0 v_p - m\Delta f \tau_p)} \mathbf{b}(\theta_{p,j}, \gamma_{p,j}) \mathbf{a}^{\text{H}}(\phi_{k,p}, r_{k,p}) \end{aligned} \quad (10)$$

where $\varepsilon_p = \alpha_{k,p} \beta_{p,j}$ and $\tau_p = \tau_{k,p} + \tau_{p,j} = (r_{k,p} + \gamma_{p,j})/c$ are the bistatic complex channel factor and bistatic propagation delay, respectively, associated with the p -th scatterer of the target, while $v_p = v_{k,p} + v_{p,j}$ is the bistatic Doppler shift whose expression will be provided in Section IV-B.

III. OFDM INPUT-OUTPUT RELATIONSHIP

The OFDM frame transmitted from Tx k to target l is given by

$$\mathbf{s}_{k,l}(t) = \mathbf{f}_l \sum_{n=0}^{N-1} \sum_{m=0}^{M-1} x_{k,l}[m, n] g_{m,n}(t) \quad (11)$$

where $\mathbf{f}_l \in \mathbb{C}^{N_{\text{rx}} \times 1}$ is a (unit-norm) transmit beamforming (in the FF) or beamfocusing (in the NF) vector to point toward l , and $x_{k,l}[m, n]$ is a generic complex modulation symbol of the $M \times N$ OFDM resource grid used at the Tx k to estimate range, angle, and velocity parameters of the target l ; $g_{m,n}(t)$ is given by

$$g_{m,n}(t) = \text{rect}\left(\frac{t - nT_0}{T_0}\right) e^{j2\pi m \Delta f (t - T_{\text{cp}} - nT_0)} \quad (12)$$

where $\text{rect}(x)$ is a pulse-shaping function taking value 1 when $0 \leq x \leq 1$ and 0 elsewhere.

The noise-free N_{rx} -dimensional continuous-time signal transmitted by the k -th Tx, scattered by the l -th ET, and received from the j -th Rx is given by

$$\begin{aligned} \mathbf{r}_{k,j}(t) &= \sum_{p=1}^P \varepsilon_p e^{j2\pi \nu_p t} \mathbf{b}(\theta_{p,j}, \gamma_{p,j}) \mathbf{a}^H(\phi_{k,p}, r_{k,p}) \mathbf{s}_{k,l}(t - \tau_p) \\ &= \sum_{p=1}^P \varepsilon_p e^{j2\pi \nu_p t} \mathbf{b}(\theta_{p,j}, \gamma_{p,j}) \mathbf{a}^H(\phi_{k,p}, r_{k,p}) \times \\ &\quad \times \mathbf{f}_l \sum_{n=0}^{N-1} \sum_{m=0}^{M-1} x_{k,l}[m, n] g_{m,n}(t - \tau_p). \end{aligned} \quad (13)$$

As previously mentioned, the Tx beamforming/beamfocusing vectors are designed to cover non-overlapping sections of the beam space. In the simultaneous presence of L (extended) targets, we assume that they are sufficiently separated in space, i.e., $|\mathbf{a}^H(\phi_{k,l}, r_{k,l}) \mathbf{f}_{l'}(\hat{\phi}_{k,l'}, \hat{r}_{k,l'})| \approx 0$ for $l' \neq l$, where $\hat{\phi}_{k,l'}$ is the pointing direction (AoD) for a Tx beamformer $\mathbf{f}_{l'}$ associated with the l' -th (extended) target.

In the following, we focus on using a single Tx beamformer such that multiple segments of the beam space are served in a time-division manner. Aiming at reducing hardware complexity and energy consumption at the radar Rx, we process the received signal $\mathbf{r}_{k,j}(t)$ by a reduction matrix before sampling. In particular, we focus the radar Rx on a single target l for B OFDM frames and estimate different targets sequentially in time. To achieve this, a reduction matrix $\mathbf{U}_b \in \mathbb{C}^{N_{\text{rx}} \times N_{\text{rx}}^{\text{rf}}}$ is chosen to cover a particular area in the beam space (determined by the current Tx beamformer). Then, after the OFDM demodulator, considering negligible inter-carrier interference (ICI) and inter-symbol interference (ISI) and including noise, a received time-frequency grid of complex elements $y[m, n]$ is obtained at each RF chain. Thus, considering the channel model in (10), the $N_{\text{rx}}^{\text{rf}} \times 1$ vector of the received complex modulation symbols for a specific block b is given by

$$\begin{aligned} \mathbf{y}_b[m, n] &= \mathbf{U}_b^H \mathbf{H}_{k,j}[m, n] \mathbf{f}_l x_{k,l}[m, n] + \mathbf{w}[m, n] \\ &= \sum_{p=1}^P \varepsilon_p \mathbf{U}_b^H \mathbf{b}(\theta_{p,j}, \gamma_{p,j}) \mathbf{a}^H(\phi_{k,p}, r_{k,p}) \times \\ &\quad \times \mathbf{f}_l x_{k,l}[m, n] e^{j2\pi(nT_0 \nu_p - m \Delta f \tau_p)} + \mathbf{w}[m, n] \end{aligned} \quad (14)$$

where $\mathbf{w} \sim \mathcal{CN}(\mathbf{0}, \sigma_w^2 \mathbf{I}_{N_{\text{rx}}^{\text{rf}}})$ is the complex Gaussian noise. By stacking the $M \times N$ OFDM symbol grid into a $MN \times$

1 vector $\underline{\mathbf{x}}_b$, where the underline symbol indicates blocked quantities, and defining $\mathbf{T}(\tau, \nu) \in \mathbb{C}^{MN \times MN}$ as

$$\begin{aligned} \mathbf{T}(\tau, \nu) &= \text{diag}([1, \dots, e^{j2\pi n T_0 \nu}, \dots, e^{j2\pi(N-1)T_0 \nu}]^T \\ &\quad \otimes [1, \dots, e^{-j2\pi m \Delta f \tau}, \dots, e^{-j2\pi(M-1)\Delta f \tau}]^T) \end{aligned} \quad (15)$$

the effective channel matrix of dimension $N_{\text{rx}}^{\text{rf}} MN \times MN$, defined for a single scatterer p is given by

$$\begin{aligned} \mathbf{G}_b(\tau_p, \nu_p, r_{k,p}, \gamma_{p,j}, \theta_{p,j}, \phi_{k,p}) &\triangleq \\ &\triangleq \mathbf{T}(\tau_p, \nu_p) \otimes \left(\mathbf{U}_b^H \mathbf{b}(\theta_{p,j}, \gamma_{p,j}) \mathbf{a}^H(\phi_{k,p}, r_{k,p}) \mathbf{f}_l \right). \end{aligned} \quad (16)$$

Since the delay parameter can be expressed as $\tau = (r + \gamma)/c$, it possible to parameterize $\mathbf{T}(\tau, \nu) \rightarrow \mathbf{T}(r, \gamma, \nu)$ and the effective channel matrix can be rewritten as

$$\begin{aligned} \mathbf{G}_b(\nu_p, r_{k,p}, \gamma_{p,j}, \theta_{p,j}, \phi_{k,p}) &\triangleq \\ &\triangleq \mathbf{T}(r_{k,p}, \gamma_{p,j}, \nu_p) \otimes \left(\mathbf{U}_b^H \mathbf{b}(\theta_{p,j}, \gamma_{p,j}) \mathbf{a}^H(\phi_{k,p}, r_{k,p}) \mathbf{f}_l \right). \end{aligned} \quad (17)$$

The received signal $\underline{\mathbf{y}}_b \in \mathbb{C}^{N_{\text{rx}}^{\text{rf}} MN \times 1}$ can then be written as

$$\underline{\mathbf{y}}_b = \sum_{p=1}^P \varepsilon_p \mathbf{G}_b(\nu_p, r_{k,p}, \gamma_{p,j}, \theta_{p,j}, \phi_{k,p}) \underline{\mathbf{x}}_b + \mathbf{w}_b. \quad (18)$$

For the derivation of the ML target parameter estimation in Section IV, we consider a single Tx and Rx pair and drop their respective indices, $(\cdot)_{k,j}$, to avoid excessive notation clutter. Needless to say, the same formulation holds for other pairs. Moreover, hereinafter we assume $N_{\text{tx}} = N_{\text{rx}} = N_a$ and $N_{\text{rx}}^{\text{rf}} = N_{\text{rf}}$.

IV. PARAMETER ESTIMATION AND DETECTION

Since we assume no a priori knowledge of the target's initial position relative to the NF/FF boundary, we introduce a *two-stage* ML parameter estimation framework. In the first stage, FF propagation conditions are assumed, which allows for a low-complexity estimation procedure. This procedure involves covering radial segments of the beam space using FF beamforming at the Tx and performing target parameter estimation based on bistatic FF assumptions at the Rx units. This scheme results in two advantages: 1) As shown in Fig. 1, covering the beam space with beamforming vectors reduces the latency resulting from codeword selection, since the FF codebook is parameterized only in angle, while the NF codebook is two-dimensional. 2) As will be shown in this section, while the parameter search space of the FF model is three-dimensional, the NF model requires a five-dimensional search space, significantly increasing the complexity of the parameter estimation procedure.

For the second stage, based on the estimates obtained from the first stage, if the target is determined to be in the NF region of either the Tx or Rx units, a second estimation stage is performed. Depending on the target being located in the NF of the Tx or Rx, the second stage will differ, as will be outlined in the following.

It is important to note that if NF conditions occur in the initial stage, the model mismatch between NF and FF array response vectors, presented in Section II-C, can lead to poor

performance in target parameter estimation. However, these approximate and inaccurate estimates are used to define a RoI for further processing based on the correct (i.e., NF) model.

A. Maximum likelihood parameter estimation

Considering the received signal in (18), we denote the true values of target parameters as $\hat{\boldsymbol{\theta}} = \{\hat{\varepsilon}_p, \hat{\nu}_p, \hat{r}_p, \hat{\gamma}_p, \hat{\theta}_p, \hat{\phi}_p\}_{p=0}^{P-1}$. For each $b \in [B]$, the effective channel matrix of dimension $N_{\text{rf}}NM \times NM$ associated with the scattering point p is given as $\mathbf{G}_b(\hat{\nu}_p, \hat{r}_p, \hat{\gamma}_p, \hat{\theta}_p, \hat{\phi}_p)$ in (17). Given the number of scattering points P , the ML estimate of the set $\hat{\boldsymbol{\theta}}$ can be obtained by solving (19), where the space is $\Gamma \triangleq \mathbb{C}^P \times \mathbb{R}^{5P}$.

Solving (19) requires knowledge of the number of scattering points P , which can be formulated as a model order estimation problem. Since the *micro-scatterers* of ETs are often indistinguishable, estimating the model order is an unattainable task because the problem is intrinsically ill-posed [32]. In addition, the parameter space of the brute-force ML solution in (19) requires prohibitively large computations. Therefore, we resort to an approximate method that evaluates a hypothesis test on a set of $(\nu, r, \gamma, \theta, \phi)$ tuples belonging to a grid Θ .

Specifically, for each point in the grid Θ , we perform a binary hypothesis test to determine whether the grid point contains a micro-scatterer (\mathcal{H}_1) or not (\mathcal{H}_0), assuming that at most one micro-scatterer is present. The corresponding log-likelihood ratio (LLR) is given by

$$\Lambda(\underline{\mathbf{y}}^{(B)}) := \log \frac{\exp\left(-\frac{1}{\sigma_w^2} \sum_{b=1}^B \left\| \underline{\mathbf{y}}_b - \varepsilon \mathbf{G}_b \mathbf{x}_b \right\|_2^2\right)}{\exp\left(-\frac{1}{\sigma_w^2} \sum_{b=1}^B \left\| \underline{\mathbf{y}}_b \right\|_2^2\right)} \quad (20)$$

where $\underline{\mathbf{y}}^{(B)} = [\underline{\mathbf{y}}_1^\top, \dots, \underline{\mathbf{y}}_B^\top]^\top$ is the vector of received symbols, obtained by accumulating all observations up to the B -th slot.

After following the derivation outlined in Appendix A and maximizing over the amplitude ε , based on the (mismatched) working assumption that the considered grid point is the sole micro-scatterer, a generalized LLR is obtained from (20) as follows

$$\ell(\nu, r, \gamma, \theta, \phi) = \frac{|\mathbf{f}^H \mathbf{a} \mathbf{b}^H \boldsymbol{\xi}_{(B)}(r, \gamma, \nu)|^2}{\mathbf{f}^H \mathbf{a} \mathbf{b}^H \bar{\mathbf{U}}_{(B)} \mathbf{b} \mathbf{a}^H \mathbf{f}} \quad (21)$$

where $\boldsymbol{\xi}_{(B)}$ and $\bar{\mathbf{U}}_{(B)}$ are defined in (42).

Then, the generalized LLR test takes on the form

$$\ell(\nu, r, \gamma, \theta, \phi) \underset{\mathcal{H}_0}{\overset{\mathcal{H}_1}{\gtrless}} T_r, \quad (\nu, r, \gamma, \theta, \phi) \in \Theta \quad (22)$$

where the threshold T_r is chosen at each grid point by using the ordered statistic constant false alarm rate (OS-CFAR) approach described in [33].⁵

Note that finding the $(\nu, r, \gamma, \theta, \phi)$ tuple that maximizes the metric in (21) corresponds to solving an ML estimation problem for a single scattering point scenario. When dealing with scenarios where multiple point-wise targets are well separated

⁵The OS-CFAR represents a well-established solution, offering very good performance, superior to other approaches, when considering multi-target and cluttered environments [34].

with respect to system resolution limits, the detection and estimation of these targets may require successive interference cancellation (SIC). In this approach, the contribution of each estimated point is removed from the signal, and the metric is re-evaluated iteratively until some stopping criteria are met (see, e.g., [5]). In ET scenarios, where micro-scatterers are often very closely spaced, the mutual interference caused by the ‘‘sidelobes’’ of the likelihood function for adjacent micro-scatterers makes the SIC approach ineffective for detecting individual micro-scatterers. On the other hand, in this work, we are not interested in precisely detecting each micro-scatterer, but rather in producing a sort of ‘‘radar image’’, i.e., a cloud of grid points detected as active and concentrated on the ET. As demonstrated in Section IV, the proposed technique (i.e., creating such a radar image by computing the LLR metric in (21)) yields very satisfactory performance. Since we assume that the target location within the NF or FF of the arrays is initially unknown, to tackle the large search space of the refined grids over Θ to obtain highly accurate estimates, we propose the two-stage ML estimation method outlined below.

Remark 4. As described in Section II, each ET in this work represents a potential communication UE (e.g., a vehicle). For this reason, the term target ‘‘detection’’ here differs from the concept of detecting the ET that can be achieved via communication. In the grided ML search described above, detection refers to distinguishing the response from a point scatterer (or multiple point scatterers that, due to system resolution limits, appear as a single point response) from noise in the radar image. This is achieved by evaluating (21) over the set of tuples on the defined grid.

Stage 1) Far-field beamforming and bistatic estimation:

In the first stage, we assume no knowledge of the target position. The appropriate FF beamforming codeword is selected at the Tx. Based on the assumption that the ET is located in the FF of both the Tx and Rx units, the array manifolds at the Tx and Rx in (17), which depend only on angular parameters (i.e., $\mathbf{a}(\phi, r) \rightarrow \mathbf{a}(\phi)$ and $\mathbf{b}(\theta, \gamma) \rightarrow \mathbf{b}(\theta)$), are considered for parameter estimation. Additionally, since the distance cannot be estimated from the array manifold in this model, it has to be estimated from the observed total time of flight, $\tau = (r + \gamma)/c$, by exploiting the subcarrier dimension of the OFDM frames, i.e., through the phase observed on the $m\Delta f\tau$ component of the exponent in (14). Moreover, the bistatic Doppler projection seen by each of the Rx units, as given in (28), can be estimated over the OFDM symbol dimension, i.e., from the phase observed on the $nT_0\nu$ component of the exponent in (14) [35]. As such, the effective channel matrix $\mathbf{G}_b(\nu_p, r_p, \gamma_p, \theta_p, \phi_p)$ in (17) takes the form

$$\check{\mathbf{G}}_b(\nu_p, \tau_p, \theta_p) \triangleq \mathbf{T}(\tau_p, \nu_p) \otimes \left(\mathbf{U}_b^H \mathbf{b}(\theta_p) \mathbf{a}^H(\phi_p) \mathbf{f}(\hat{\phi}_p) \right). \quad (23)$$

Note that, from the bistatic Rx’s perspective, the channel response from Tx to the target is a constant that can be absorbed in the channel gain coefficient, i.e. :

$$g_p \triangleq \mathbf{a}^H(\phi_p) \mathbf{f}(\hat{\phi}_p), \quad h_p \triangleq g_p \varepsilon_p$$

$$\boldsymbol{\theta}_{\text{ML}} = \underset{\{\varepsilon_p, v_p, r_p, \gamma_p, \theta_p, \phi_p\}_{p=0}^{P-1} \in \Gamma}{\arg \min} \left\| \sum_{b=0}^{B-1} \mathbf{y}_b - \sum_{p=0}^{P-1} \varepsilon_p \mathbf{G}_b(v_p, r_p, \gamma_p, \theta_p, \phi_p) \mathbf{x}_b \right\|_2^2 \quad (19)$$

and therefore, $\check{\mathbf{G}}_b$ is not a function of the AoD, ϕ . Then, defining the true values of parameters as $\check{\boldsymbol{\theta}} = \{\check{h}_p, \check{v}_p, \check{r}_p, \check{\theta}_p\}_{p=0}^{P-1}$, the received signal takes the form

$$\underline{\mathbf{y}}_b = \sum_{p=0}^{P-1} \check{h}_p \check{\mathbf{G}}_b(\check{v}_p, \check{r}_p, \check{\theta}_p) \mathbf{x}_b + \mathbf{w}_b. \quad (24)$$

For an ET with P scattering points, the ML estimate of the set $\check{\boldsymbol{\theta}}$ involves a search in a $\Gamma_{\text{FF}} \triangleq \mathbb{C}^P \times \mathbb{R}^{3P}$ space. The likelihood function for the FF model is obtained similarly to the approach in Appendix A (details omitted for brevity). In this case, by maximizing the log-likelihood function with respect to h_p , we obtain

$$\ell(v, \tau, \theta) = \frac{|\mathbf{b}^H(\theta) \boldsymbol{\xi}_{(B)}(\tau, v)|^2}{\mathbf{b}^H(\theta) \bar{\mathbf{U}}_{(B)} \mathbf{b}(\theta)}. \quad (25)$$

By defining a suitably refined search grid on $\Theta_{\text{FF}} \triangleq \mathbb{R}^{3P}$, evaluating (25) for every tuple $(v, \tau, \theta) \in \Theta_{\text{FF}}$, and performing the estimation and detection (thresholding) step according to Section IV-A, the estimates $(\hat{v}, \hat{\tau}, \hat{\theta})$ of the scattering points can be obtained. To convert these values to the angle and range of the target in the global coordinates, we use the bistatic conversion principles in the next section.

B. Bistatic range and Doppler shift

In a bistatic configuration, the propagation time τ_p of the signal scattered by a scatterer p is related to the distance between the Tx and the scatterer, $r_{\text{tx},p}$, and that between the scatterer and the Rx, $\gamma_{p,\text{rx}}$, via the bistatic range, $R_{\text{bis}} = r_{\text{tx},p} + \gamma_{p,\text{rx}} = \tau_p \cdot c$ [35]. After estimating R_{bis} via τ_p , the scatterer can be located on an ellipse with a major axis equal to R_{bis} and foci at Tx and Rx positions, as depicted in the inset of Fig. 3. The Tx, Rx, and scatterer form a triangle with base Δ (with Δ the distance between Tx and Rx) called the baseline; the angle β of the opposite vertex is named the bistatic angle.

If the AoA $\theta_{p,\text{rx}}$ of the reflected echo at the Rx can be estimated, it is possible to determine the distance γ as [36]

$$\gamma_{p,\text{rx}} = \frac{R_{\text{bis}}^2 - \Delta^2}{2(R_{\text{bis}} + \Delta \sin(\theta_{p,\text{rx}} - \pi/2))} \quad (26)$$

and then the scatterer position with respect to the Rx local reference system

$$\mathbf{p}_p = [\gamma_{p,\text{rx}} \cos \theta_{p,\text{rx}}, \gamma_{p,\text{rx}} \sin \theta_{p,\text{rx}}]^T. \quad (27)$$

In addition to the scatterer location, the bistatic velocity v_{bis} of the scatterer can be inferred from the bistatic Doppler shift. The latter is proportional to the rate of change of R_{bis} . When

Tx and Rx are stationary, and the scatterer is moving with velocity \mathbf{v}_p , the Doppler shift can be obtained as [36]

$$\begin{aligned} v_p &= v_{\text{tx},p} + v_{p,\text{rx}} \\ &= \frac{1}{\lambda_c} \frac{d}{dt} [r_{\text{tx},p}(t) + \gamma_{p,\text{rx}}(t)] = \frac{2s_p}{\lambda_c} \cos \delta \cos(\beta/2) \end{aligned} \quad (28)$$

where $\lambda_c = c/f_c$ is the wavelength, δ is the angle between the direction of the velocity and the bistatic bisector, and $s_p = |\mathbf{v}_p|$. While β can be easily determined by knowing Δ , $r_{\text{tx},p}$, $\gamma_{p,\text{rx}}$, and $\theta_{p,\text{rx}}$, the angle δ is unknown so only the bistatic velocity component in (28), i.e., $v_{\text{bis}} = |\mathbf{v}_{\text{bis}}| = s_p \cos \delta$, can be estimated by the system.

Stage 2) Near-field estimation: The second stage is only carried out if the target is determined to be in the NF of the Tx or Rx units, based on the estimates obtained by evaluating the FF model in (25). The second stage is described below for each scenario.

Near-field of Rx: Parameter estimation with reduced search space. Assume the target is determined to lie in the NF of an Rx array. This means the metric in (21) needs to be evaluated on a fine-grained grid defined over Θ to meet high-accuracy localization requirements. It is clear that evaluating a 5-D search grid is computationally heavy. Therefore, we define a suitably refined Cartesian grid over the RoI, indicated by the approximate estimates from the first stage. Subsequently, the coordinates of each cell in the grid are translated to the equivalent $(r_p, \gamma_p, \theta_p, \phi_p)$ and the LLR metric in (21) is evaluated.

Discussion: Note that the transition region between NF and FF does not have a hard cut-off. FF beams already start to form after approximately $D_{\text{ff}}/10$ [17], [13], albeit with some phase variations. As the radial distance from the array approaches this boundary, the array manifold tends increasingly toward the FF model. This is important because if a target is located in these transitional regions, it is not critical to determine whether it is in the NF or FF regime. In fact, even the FF model will yield acceptable performance for parameter estimation and beamforming. This effect is also evident from the numerical results in Section VI-D, where the beamforming and beamfocusing schemes exhibit similar performance in these regions.

Near-field of Tx: Beamfocusing and re-estimation.

As mentioned in Section II-B, if the target is determined to be in the NF of a Tx array, using a beamforming approach to illuminate it results in a loss of performance due to the considered mismatched array response. In other words, the beamformer at the Tx cannot focus the energy at the intended location with full beamforming gain. In this case, a codeword from a custom-designed beamfocusing codebook is selected to illuminate the area estimated by the first stage. These codewords are designed (see Section V for details) to

maintain a constant gain in an extended region (angle-range). This scheme provides a three-fold advantage: 1) Due to the increase in beamforming gain (and therefore higher SNR) after selecting the appropriate codeword, a re-estimation of the target parameters at the Rx leads to more accurate estimates. Note that, in this case, the Rxs can use the FF model due to the deployment topology (see Fig. 3). 2) Communication performance can be significantly increased for the considered case where the target is also a communication user. 3) Utilizing the aforementioned codebook allows the system to focus on a limited number of range-angle spots—even just one—within the identified region, thus drastically reducing the computational burden. In contrast, traditional beamfocusing methodologies that rely on designing weights by conjugating the array response can require exploring multiple distances for each angle after the first estimation round, thus significantly increasing the computational complexity. Since beamfocusing can illuminate an extended region with a constant gain, even if the true UE antenna location deviates slightly from the one estimated from the back-reflected signal, a good SNR can still be maintained. We further remark that, if the RoI for the second stage is larger than the area covered by the NF codeword, multiple neighboring codewords can be used in a time-division manner to cover the RoI for re-estimation.

V. DESIGN OF THE BEAMFOCUSING WEIGHTS

Algorithm 1 Algorithm for designing beamfocusing vectors

for codeword $g \in \mathcal{C}_f$ **do**

- 1) choose solution tolerance ϱ , Tikhonov regularizer ϵ_T , set $\mathbf{c}_g = e^{j*0_G}$
- 2) initialize \mathbf{f}_g ▷ see **Initialization**
- 3) set \mathbf{c}_g to $\mathbf{c}_g = e^{j\angle(\mathbf{A}^H \mathbf{f}_g)}$
- 4) fix \mathbf{c}_g , update new \mathbf{f}_g by obtaining the residual error from evaluating the unconstrained linear least-squares problem, $\|\mathbf{b}_g - |\mathbf{A}^H \mathbf{f}_g|\|_2$.
- 5) repeat steps (2 - 4) until the decrease in objective function has diminished to within ϱ .

end for

Initialization

$\mathbf{y}' \leftarrow \mathbf{y}_g \odot \mathbf{c}_g$ ▷ \mathbf{y}_g is the mask corresponding to \mathbf{f}_g
 $\mathbf{f}_g \leftarrow (\mathbf{A}\mathbf{A}^H + \epsilon_T \mathbf{I}_{N_a})^{-1} \mathbf{A} \mathbf{y}'$

A. Problem formulation

Let \mathbf{f} be a beamfocusing vector of dimension N_a . The complex-valued (amplitude and phase) beam pattern radiated by the array at each sampling tuple $(\tilde{\phi}_i, \tilde{r}_j)$, $i \in [G_\phi]$, $j \in [G_r]$ of a discrete angular set $\{\tilde{\Omega}\}$, ($|\tilde{\Omega}| = G_\phi$) and range set $\{\tilde{\Gamma}\}$, ($|\tilde{\Gamma}| = G_r$) can be calculated as the inner product of the beamfocusing vector \mathbf{f} and the array response vector $\mathbf{a}(\phi, r)$ at the given grid angle-range tuple i.e., $\mathbf{a}^H(\tilde{\phi}_i, \tilde{r}_j)\mathbf{f}$.

The design problem of interest is to find \mathbf{f} to approach a desired radiation pattern $\bar{\mathbf{b}} \in \mathbb{R}_+^G$, also referred to as reference mask. The entries of the vector $\bar{\mathbf{b}} = [\bar{b}_1, \dots, \bar{b}_G]$,

represent the magnitudes of the radiation pattern at each of the $G = G_\phi G_r$ discrete tuple points. In particular, we fix $\bar{\mathbf{b}}$ to have a constant level in a pre-determined angle-range zone (i.e., spot) in the NF of the array and such that the values corresponding to the rejection directions (sidelobes) are below a certain threshold with respect to the maximum (center beam). By letting $\mathbf{A} = [\mathbf{a}(\tilde{\phi}_1, \tilde{r}_1), \dots, \mathbf{a}(\tilde{\phi}_{G_\phi}, \tilde{r}_{G_r})] \in \mathbb{C}^{N_a \times G}$, this problem can be formulated as a magnitude least-squares problem, which belongs to the class of problems addressed by [37], [38], as follows

$$\begin{aligned} \min_{\mathbf{f}} \quad & \|\mathbf{A}^H \mathbf{f} - \bar{\mathbf{b}}\|_2^2 \\ \text{s.t.} \quad & \mathbf{f}^H \mathbf{A} \mathbf{A}^H \mathbf{f} = 1 \end{aligned} \quad (29)$$

where the constraint in (29) imposes unit transmit power. Depending on the operating scenario, a beam pattern can focus the transmitted energy on a certain given angle-range sector (i.e., field of view (FoV) equal to $\Omega \times \Gamma$). In order to define our design in a flexible manner, the FoV is divided into multiple sectors as depicted in Fig. 1b, each sector determining the illumination area of a codeword (i.e., the span of the beamfocusing *spots*). These codewords are gathered in a codebook \mathcal{C}_f . Note that the problem in (29) aims to approximate the magnitude of the reference mask, which gives a less constrained solution, compared to the phase and magnitude counterpart, i.e., without the absolute value operator. Problem in (29) is not convex. However, by performing a semidefinite relaxation, good feasible solutions can be obtained.

In particular, we resort to the iterative method detailed in Alg. 1. Note that due to the fine-grained grid used for the sampling points (i.e., G_r, G_ϕ) of the array manifold matrix \mathbf{A} , this matrix may not be full rank (i.e., $\text{rank}(\mathbf{A}) < \#\text{cols}(\mathbf{A})$). To overcome this problem, we use *Tikhonov* regularization with parameter $\epsilon_T \in \mathbb{R}_+$. A detailed description of Alg. 1 with regularization is provided in an online version of this document [39]. Two examples of the obtained beamfocusing radiation patterns and the corresponding masks are shown in Fig. 4.

Remark 5. The masks $\bar{\mathbf{b}} \in \mathbb{R}_+^G$ as defined above, consist of sharp transitions from the desired focusing spot to the rejection region outside the spot. These transitions can lead to “ripples”, analogous to the phenomenon observed in standard digital filter design. Moreover, due to the nonlinearity of wave propagation, beamfocusing patterns for masks that are “wide and long” (i.e. large span in angle and range) are difficult to synthesize. To mitigate these problems, a possible solution borrowed from digital filter design consists of using *windowing* functions on the mask (e.g., Kaiser, Dolph-Chebyshev, to name a few) to create a smoother transition and better concentrate the radiated energy. More details can be found in [39].

VI. SIMULATION RESULTS

In this section, we present numerical results to evaluate the effectiveness of the proposed schemes, using the system parameters listed in Tab. I. The results in this section are based on the scenario and topology in Fig. 3, where we consider numerous trajectories, enumerated I-IV, to simulate

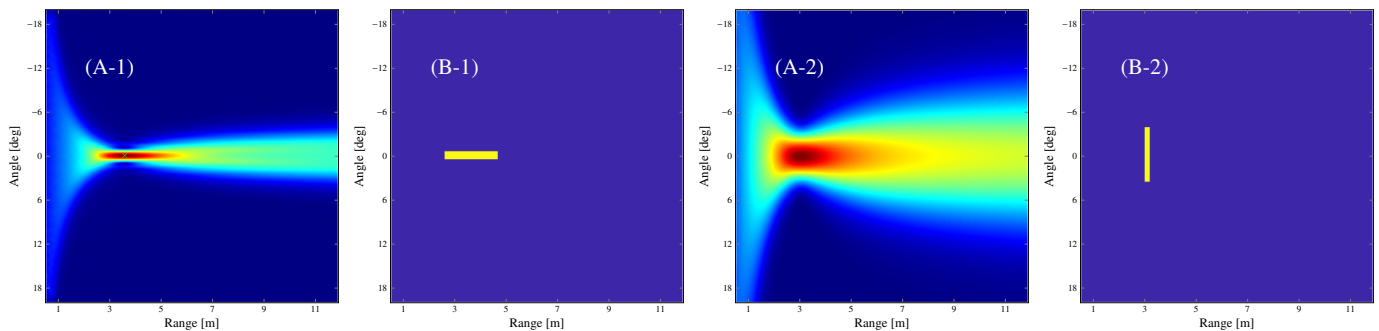


Fig. 4: Examples of beamfocusing codewords (A-X) and corresponding masks (B-X). Note that the masks are defined either to concentrate the radiated energy over extended distances (left) or an extended angular span (right).

different conditions that may be encountered in a real-world deployment. Unless otherwise stated, at each location along the trajectories, we consider an instance of the ET generated according to the BND in Section II-A and with the dimensions provided in Tab. II. Note that the grids defined for parameter estimation do not coincide with the grid used in Section II-A and Tab. II to simulate the BND ET.

A. Far-field estimation performance (Trajectory I)

Referring to Fig. 3, the ET moving along Trajectory I is located entirely in the FF of the Tx and both Rx arrays. Fig. 5 shows the estimated spatial parameters of the ET. At each step, the ET is generated 100 times in Monte Carlo (MC) fashion, independently for each of the Rx units. The boxes indicate all point estimates that pass the OS-CFAR threshold and have an amplitude within 3 dB of the main peak, local to each Rx. These bounding boxes are obtained as the minimum box that fits the convex hull contacting the above-mentioned detection points. Since the main peak in the angle/range domain from the metric in (25) is wide and leaks into the neighboring bins, the points on this main peak also pass the OS-CFAR and lead to enlarged boxes. The system parameters considered in the simulations lead to a bistatic range resolution of approximately 2.34 m and angular resolution of approximately 2.2° , which are clearly inadequate to resolve the individual scatters in the simulated target box in most cases. Therefore, after thresholding, a weighted estimate of the detected points can be computed, where each estimated point is weighted by the value obtained from evaluating (25). Then, the weighted average estimate of the target is obtained and plotted in Fig. 5 as the crosses and circles. From this, it can be observed that the estimated target location is very accurate. Note that up to an extent, super-resolution techniques (e.g., sub-space-based methods) can be used alternatively, however, this is out of scope for this paper. To further demonstrate the accuracy of the FF estimation, we calculate the root mean square error (RMSE) between the *main* peak at each iteration of the MC process and the center of the box (target). This is plotted in Fig. 5(b).

B. Multistatic spatial diversity gain (Trajectory IV)

In this setup, we aim to demonstrate the effectiveness of multistatic configurations. More specifically, it is well known

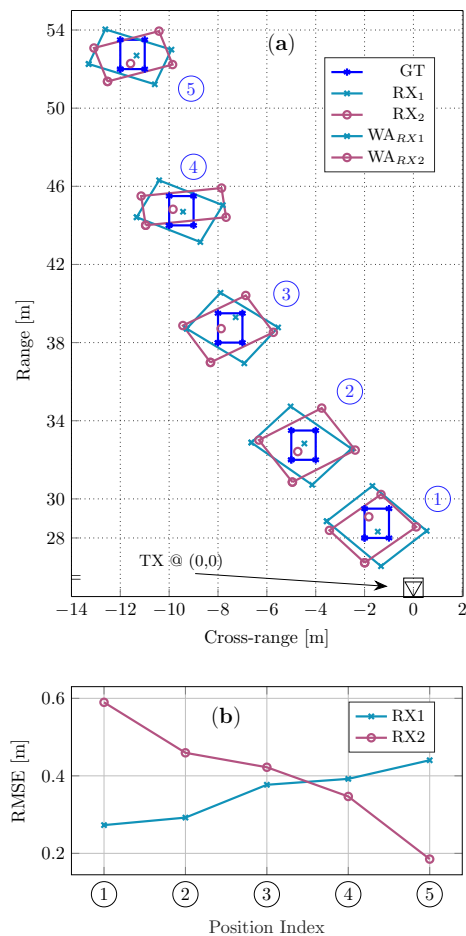


Fig. 5: FF estimates of the ET along trajectory I in Fig. 3.

that in multistatic configurations, targets observed by the Rx units from different aspect angles can exhibit significantly different reflection characteristics [40]. To this end, having multiple Rx's increases detection robustness. Given that an important distinction of radar systems utilizing multiple radars is to incorporate some level of data fusion between the measurement of individual sensors, we perform the following experiment to demonstrate this. Fig. 6 depicts the average detection probability of the considered ET at each Rx, simulated 200 times for each Rx at the given points along Trajectory IV in Fig. 3. The detection is performed locally at each Rx

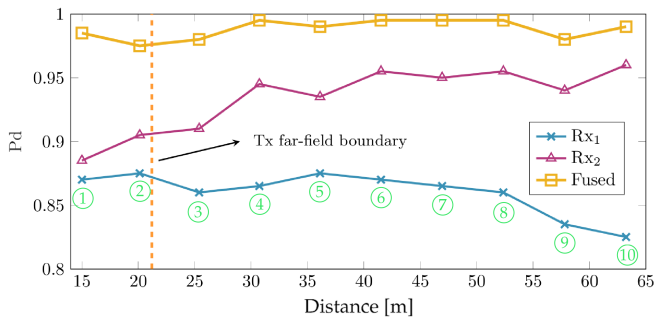


Fig. 6: Probability of detection for an ET along trajectory IV in Fig. 3. The x-axis indicates the radial distance from the Tx.

using the OS-CFAR thresholding technique. In particular, a detection is declared if the main peak passes the threshold and the estimated position resulting from the peak value satisfies $\sqrt{(\hat{x}_p - x_p)^2 + (\hat{y}_p - y_p)^2} < 1$ m. Important to note that, each realization is performed according to the BND. This means that in some instances an Rx may observe very few or even zero scattering points from the ET. The *fused* curve shows the average detection probability when, at each step, at least one of the Rxs has detected the target (i.e., an OR operation). This fusion can be performed at a central node.

C. Estimation of targets in receiver NF (Trajectory III)

In Fig. 3, the ET moving along Trajectory III is initially estimated to lie in the NF of Rx₁. Fig. 7 shows the estimates obtained from using the FF mismatched model (evaluating (25)) at the first stage. Then by defining a RoI based on these estimates, we evaluate (21) on a fine-grained grid defined over the RoI, comprising a 6×6 m² square with 0.05 m pixels. Fig. 7a corresponds to the closer target location on the trajectory, where it can be observed that it is possible to individually resolve many of the scattering points with high accuracy (much superior to the bandwidth imposed range resolution). Fig. 7b depicts the same procedure, however since the target is now further from Rx₁, the individual scattering points can not be resolved. Nonetheless, the estimated location is highly accurate. Note that the estimates obtained by Rx₂ for both positions correspond to the FF model and since the target lies in its FF, the estimates are accurate within the system limits (i.e., range and angular resolution).

D. Spectral efficiency enhancement with beamfocusing (Trajectory II)

By considering a LoS channel with free-space path loss $PL = (4\pi r/\lambda)^2$, the matching gain G_M and achievable spectral efficiency are respectively given by

$$G_M = |\mathbf{a}^H(r_0, \phi_0)\mathbf{f}_X(\hat{r}, \hat{\phi})| \quad (30a)$$

$$SE = \log_2 \left(1 + \frac{P_{\text{avg}} G_M^2}{N_0 W} \left(\frac{\lambda}{4\pi r_0} \right)^2 \right) \quad (30b)$$

with (r_0, ϕ_0) being the true location of the target, and the parameter values specified in Tab. I. $\mathbf{f}_X \in \{\mathbf{f}_N, \mathbf{f}_F\}$ is the Tx beamforming (/beamfocusing) vector where $\mathbf{f}_F(\hat{\phi})$ is a

TABLE I: System parameters

$M = 100$	$N = 6$
$f_c = 28.0$ GHz	$W = 128$ MHz
$P_{\text{avg}} = 26$ dBm	$\sigma_{\text{rscs}} = 1$ m ² , $P_{\text{fa}} = 10^{-3}$
Noise Figure (NF) = 3 dB	Noise PSD = $2 \cdot 10^{-21}$ W/Hz
$N_a = 64$	$N_{\text{rf}} = 8$, $B = 1$

TABLE II: Target parameters (see Fig. 2)

Max. length $T_l = 1.5$ m	Max. width $T_w = 1$ m
BNM parameter $q \approx 0.01$	Grid size $T_g = 0.1$ m

codeword chosen from a discrete *Fourier* codebook $\in \mathbb{C}^{N_a \times N_a}$, as the codeword with the closest angular distance of the main lobe peak with respect to the estimated AoD $\hat{\phi}$.

$\mathbf{f}_N(\hat{r}, \hat{\phi})$ is a codeword from the *custom-designed* codebook of beamfocusing vectors, as explained in Section V.

Fig. 8 shows the achievable spectral efficiency (SE) for the ET along Trajectory II. The plot is obtained by calculating the SE at a hypothetical user antenna that is mounted on the ET. Since the custom beamfocusing vectors are designed to cover an extended area with a constant gain, as in Fig. 1b, if the antenna position deviates from the expected location, the Fourier codeword performs significantly worse than beamfocusing words. To demonstrate the parameter estimation performance with beamfocusing and beamforming more explicitly, we consider a single-point scatterer at each of the locations along Trajectory II and perform parameter estimation (at Rx) using beamformed and beamfocused transmission. The results in Fig. 9 indicate an improved parameter estimation when performing beamfocusing in the NF of the Tx, which can be attributed to the increase in SNR at the target location.

VII. CONCLUSION

In this work, we have proposed a two-stage parameter estimation framework for ISAC in a multistatic configuration. The framework performs beamforming and ML parameter estimation based on the FF assumption in the first stage. The second stage of the scheme is deployed when the estimation results of the first stage indicate the sensing target to be located in the NF of the arrays. In particular, if the target is located in the NF of the Rx arrays, a high-dimensional ML parameter estimation based on the exact signal model (i.e., exact array response model) is carried out in a defined RoI. If the target is determined to be in the NF of the Tx array, the scheme selects beamfocusing codewords, which are designed by solving a magnitude least squares problem, to illuminate the target. Then, the Rx units re-estimate the target parameters.

APPENDIX A

DERIVATION OF THE LOG-LIKELIHOOD RATIO

In this appendix, we derive the generalized LLR test of the two hypotheses \mathcal{H}_1 and \mathcal{H}_0 , under the assumptions mentioned in Section IV-A. For ease of notation, we drop some of the arguments.

Given the vector of unknown parameters $\boldsymbol{\theta}_p = \{\varepsilon_p, \nu_p, r_p, \gamma_p, \theta_p, \phi_p\} \in \Gamma_p \triangleq \mathbb{C} \times \mathbb{R}^5$, the LLR of the vector of received symbols $\underline{\mathbf{y}}^{(B)} = [\underline{\mathbf{y}}_1^T, \dots, \underline{\mathbf{y}}_B^T]^T$, obtained

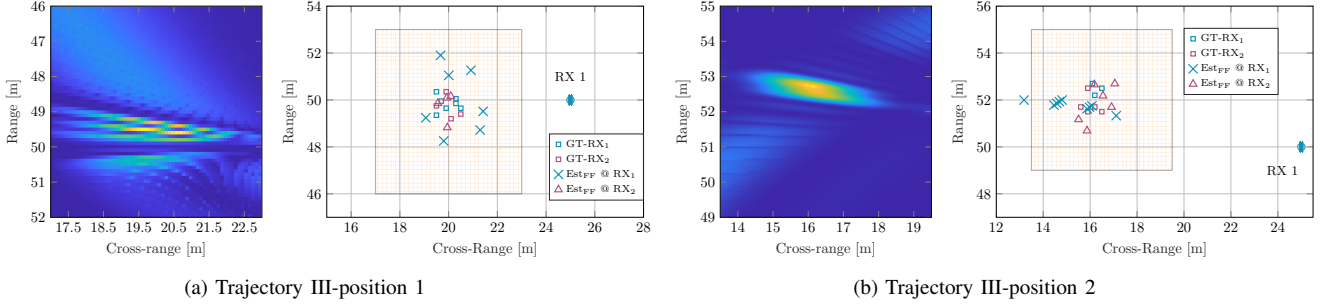


Fig. 7: The figure shows an ET located in the NF of RX₁ (Trajectory III of Fig. 3). After performing ML estimation based on FF-bistatic assumptions, the estimated scattering points from RX₁ indicate the target to be in the NF of this Rx unit. Then, a fine-grained search grid is defined in the indicated RoI, where the LLR metric in (21) is evaluated for each grid point, as shown in (b).

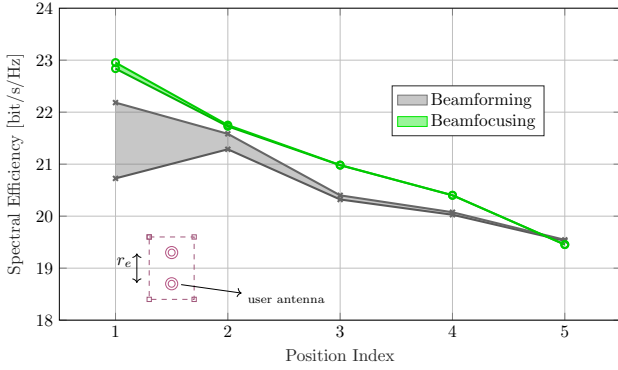


Fig. 8: Spectral efficiency achieved through beamfocusing and beamforming for an ET (UE) along trajectory II in Fig. 3. Target locations are indexed 1–5. The filled area shows the gain within a mismatched antenna distance $r_e = 1$ m on the extended object.

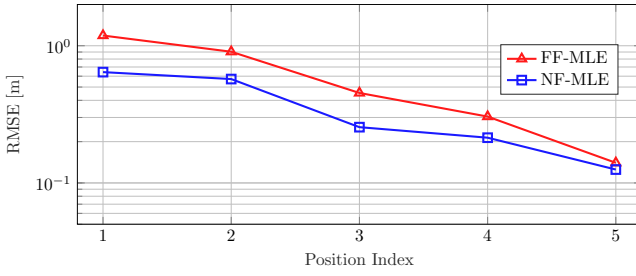


Fig. 9: Comparison of the estimation error of the target position using a NF codeword and FF codeword.

by accumulating all observations up to the B -th slot, is given by

$$\Lambda(\underline{\mathbf{y}}^{(B)}) := \log \frac{\prod_{b=1}^B L(\underline{\mathbf{y}}_b | \mathcal{H}_1, \theta_p)}{\prod_{b=1}^B L(\underline{\mathbf{y}}_b | \mathcal{H}_0)} = \ell(\underline{\mathbf{y}}^{(B)} | \mathcal{H}_1, \theta_p) - \ell(\underline{\mathbf{y}}^{(B)} | \mathcal{H}_0) \quad (31)$$

where $L(\underline{\mathbf{y}}_b | \mathcal{H}_1, \theta_p)$ is the likelihood-function of $\underline{\mathbf{y}}_b$ in (18) under the hypotheses \mathcal{H}_1 , considering the assumption that at most one micro-scatterer p is present in each cell of the grid

of points Θ . This is given by

$$L(\underline{\mathbf{y}}_b | \mathcal{H}_1, \theta_p) = \frac{1}{\det(\pi \sigma_w^2 \mathbf{I}_{NMN_{\text{rf}}})} \times \exp\left(-\frac{1}{\sigma_w^2} \left\| \underline{\mathbf{y}}_b - \varepsilon_p \mathbf{G}_b(v_p, r_p, \gamma_p, \theta_p, \phi_p) \underline{\mathbf{x}}_b \right\|_2^2\right). \quad (32)$$

From (32), dropping a few terms that are not relevant, we get

$$\ell(\underline{\mathbf{y}}^{(B)} | \mathcal{H}_1, \theta_p) = \sum_{b=1}^B \log\left(L(\underline{\mathbf{y}}_b | \mathcal{H}_1, \theta_p)\right) = -\frac{1}{\sigma_w^2} \sum_{b=1}^B \left\| \underline{\mathbf{y}}_b - \varepsilon_p \mathbf{G}_b(v_p, r_p, \gamma_p, \theta_p, \phi_p) \underline{\mathbf{x}}_b \right\|_2^2. \quad (33)$$

Moreover, $L(\underline{\mathbf{y}}_b | \mathcal{H}_0)$ is the likelihood-function of $\underline{\mathbf{y}}_b$ under the hypotheses \mathcal{H}_0 , i.e., no micro-scatterer is present in the considered cell, given by

$$L(\underline{\mathbf{y}}_b | \mathcal{H}_0) = \frac{1}{\det(\pi \sigma_w^2 \mathbf{I}_{NMN_{\text{rf}}})} \exp\left(-\frac{1}{\sigma_w^2} \left\| \underline{\mathbf{y}}_b \right\|_2^2\right). \quad (34)$$

From (34), we have

$$\ell(\underline{\mathbf{y}}^{(B)} | \mathcal{H}_0) = \sum_{b=1}^B \log\left(L(\underline{\mathbf{y}}_b | \mathcal{H}_0)\right) = -\frac{1}{\sigma_w^2} \sum_{b=1}^B \left\| \underline{\mathbf{y}}_b \right\|_2^2. \quad (35)$$

From (31), the generalized LLR test can be computed as

$$\ell(\underline{\mathbf{y}}^{(B)} | \mathcal{H}_1, \hat{\theta}_p) - \ell(\underline{\mathbf{y}}^{(B)} | \mathcal{H}_0) \underset{\mathcal{H}_0}{\overset{\mathcal{H}_1}{\gtrless}} T_r \quad (36)$$

where T_r is the threshold that is determined at each grid point by using an OS-CFAR approach, and $\hat{\theta}_p$ is the ML estimate of the vector of unknown parameters, θ_p [41]

$$\hat{\theta}_p = \underset{\varepsilon_p, v, r, \gamma, \theta, \phi}{\operatorname{argmax}} \ell(\underline{\mathbf{y}}^{(B)} | \mathcal{H}_1, \theta_p). \quad (37)$$

For a given $(v_p, r_p, \gamma_p, \theta_p, \phi_p)$ tuple, the value $\hat{\varepsilon}_p$ which maximizes (37) is given in closed form as

$$\hat{\varepsilon}_p = \frac{\sum_{b=1}^B \underline{\mathbf{x}}_b^H \mathbf{G}_b^H \underline{\mathbf{y}}_b}{\sum_{b=1}^B \underline{\mathbf{x}}_b^H \mathbf{G}_b^H \mathbf{G}_b \underline{\mathbf{x}}_b}. \quad (38)$$

Let $\mathbf{Y}_b = [\mathbf{y}_b[0, 0], \dots, \mathbf{y}_b[N-1, M-1]] \in \mathbb{C}^{N_{\text{tr}} \times NM}$, and let

$$\begin{aligned} \mathbf{G}_b^H \mathbf{G}_b &= \left(\mathbf{T} \otimes \mathbf{U}_b^H \mathbf{b} \mathbf{a}^H \mathbf{f} \right)^H \left(\mathbf{T} \otimes \mathbf{U}_b^H \mathbf{b} \mathbf{a}^H \mathbf{f} \right) \\ &\stackrel{(a)}{=} \left(\mathbf{T}^H \mathbf{T} \otimes \mathbf{f}^H \mathbf{a} \mathbf{b}^H \mathbf{U}_b \mathbf{U}_b^H \mathbf{b} \mathbf{a}^H \mathbf{f} \right) \\ &= \mathbf{f}^H \mathbf{a} \mathbf{b}^H \mathbf{U}_b \mathbf{U}_b^H \mathbf{b} \mathbf{a}^H \mathbf{f} \mathbf{I}_{NM} \end{aligned} \quad (39)$$

and

$$\begin{aligned} \mathbf{G}_b^H \mathbf{y}_b &= \left(\mathbf{T} \otimes \mathbf{U}_b^H \mathbf{b} \mathbf{a}^H \mathbf{f} \right)^H \mathbf{y}_b = \left(\mathbf{T}^H \otimes \mathbf{f}^H \mathbf{a} \mathbf{b}^H \mathbf{U}_b \right) \mathbf{y}_b \\ &\stackrel{(b)}{=} \mathbf{T}^H \mathbf{Y}_b^T \mathbf{U}_b^T \mathbf{b}^* \mathbf{a}^T \mathbf{f}^* \end{aligned} \quad (40)$$

where (a) stems from the mixed-product property of the Kronecker product: $(\mathbf{A} \otimes \mathbf{B})(\mathbf{C} \otimes \mathbf{D}) = (\mathbf{AC} \otimes \mathbf{BD})$, (b) from the mixed Kronecker matrix-vector product: $(\mathbf{A} \otimes \mathbf{r})\text{vec}(\mathbf{V}) = \mathbf{AV}^T \mathbf{r}^T$, where $\text{vec}(\cdot)$ is an operator used to transform a matrix into a column vector. By replacing (39) and (40) in (38), the channel coefficient estimator can be rewritten as

$$\hat{\epsilon}_p = \frac{\mathbf{f}^H \mathbf{a} \mathbf{b}^H \boldsymbol{\xi}_{(B)}(r_p, \gamma_p, \nu_p)}{\mathbf{f}^H \mathbf{a} \mathbf{b}^H \bar{\mathbf{U}}_{(B)} \mathbf{b} \mathbf{a}^H \mathbf{f}} \quad (41)$$

where the following definitions are used:

$$\begin{aligned} \bar{\mathbf{U}}_{(B)} &= \sum_{b=1}^B \|\mathbf{x}_b\|_2^2 \mathbf{U}_b \mathbf{U}_b^H \\ \boldsymbol{\xi}_{(B)}(r_p, \gamma_p, \nu_p) &= \left[\sum_{b=1}^B \mathbf{x}_b^T \mathbf{T}(r_p, \gamma_p, \nu_p) \mathbf{Y}_b^H \mathbf{U}_b^H \right]^H. \end{aligned} \quad (42)$$

Lastly, by substituting (41) into (33), we get

$$\begin{aligned} \ell(\underline{\mathbf{y}}^{(B)} | \mathcal{H}_1, \hat{\boldsymbol{\theta}}_p) &= \\ &= -\frac{1}{\sigma_w^2} \left(\sum_{b=1}^B \|\mathbf{y}_b\|_2^2 - \frac{|\mathbf{f}^H \mathbf{a} \mathbf{b}^H \boldsymbol{\xi}_{(B)}(r_p, \gamma_p, \nu_p)|^2}{\mathbf{f}^H \mathbf{a} \mathbf{b}^H \bar{\mathbf{U}}_{(B)} \mathbf{b} \mathbf{a}^H \mathbf{f}} \right). \end{aligned} \quad (43)$$

Then, going back to (36), the generalized LLR test, given in (22), for a generic scatterer parameter tuple $(\nu, r, \gamma, \theta, \phi)$ can be obtained as follows

$$\ell(\nu, r, \gamma, \theta, \phi) = \frac{|\mathbf{f}^H \mathbf{a} \mathbf{b}^H \boldsymbol{\xi}_{(B)}(r, \gamma, \nu)|^2}{\mathbf{f}^H \mathbf{a} \mathbf{b}^H \bar{\mathbf{U}}_{(B)} \mathbf{b} \mathbf{a}^H \mathbf{f}} \underset{\mathcal{H}_0}{\overset{\mathcal{H}_1}{\gtrless}} T_r \quad (44)$$

where the search space is $\Theta_{\text{ML}} \triangleq \mathbb{R}^{5P}$.

REFERENCES

- [1] D. K. P. Tan, J. He, Y. Li, A. Bayesteh, Y. Chen, P. Zhu, and W. Tong, "Integrated sensing and communication in 6G: Motivations, use cases, requirements, challenges and future directions," in *2021 1st IEEE International Online Symposium on Joint Communications & Sensing (JC&S)*, Dresden, Germany, Feb. 2021, pp. 1–6.
- [2] F. Liu, Y. Cui, C. Masouros, J. Xu, T. X. Han, Y. C. Eldar, and S. Buzzi, "Integrated sensing and communications: Toward dual-functional wireless networks for 6G and beyond," *IEEE J. Sel. Areas Commun.*, vol. 40, no. 6, pp. 1728–1767, June 2022.
- [3] M. Braun, C. Sturm, and F. K. Jondral, "Maximum likelihood speed and distance estimation for OFDM radar," in *Proc. IEEE Radar Conf.*, Arlington, VA, USA, May 2010, pp. 256–261.
- [4] C. B. Barneto, T. Riihonen, M. Turunen, L. Anttila, M. Fleischer, K. Stadius, J. Ryyänen, and M. Valkama, "Full-duplex OFDM radar with LTE and 5G NR waveforms: challenges, solutions, and measurements," *IEEE Trans. Microw. Theory Tech.*, vol. 67, no. 10, pp. 4042–4054, Oct. 2019.
- [5] S. K. Dehkordi, L. Gaudio, M. Kobayashi, G. Caire, and G. Colavolpe, "Beam-space MIMO radar for joint communication and sensing with OTFS modulation," *IEEE Trans. Wireless Commun.*, vol. 22, no. 10, pp. 6737–6749, Oct. 2023.
- [6] L. Pucci, E. Paolini, and A. Giorgetti, "System-level analysis of joint sensing and communication based on 5G new radio," *IEEE J. Sel. Areas Commun.*, vol. 40, no. 7, pp. 2043–2055, July 2022.
- [7] O. Kanhere, S. Goyal, M. Beluri, and T. S. Rappaport, "Target localization using bistatic and multistatic radar with 5G NR waveform," in *Proc. 2021 IEEE 93rd Vehicular Technology Conference (VTC2021-Spring)*, Helsinki, Finland, April 2021, pp. 1–7.
- [8] K. Abratkiewicz, A. Księżyk, M. Plotka, P. Samczyński, J. Wszolek, and T. P. Zielinski, "SSB-based signal processing for passive radar using a 5G network," *IEEE J. Sel. Top. Appl. Earth Obs. Remote Sens.*, vol. 16, pp. 3469–3484, Mar. 2023.
- [9] A. Schwind, C. Andrich, P. Wendland, M. Döbereiner, G. Del Galdo, G. Schaefer, R. S. Thomä, and M. A. Hein, "Bi-static delay-doppler emulation of cooperative passive vehicle-to-X radar," in *Proc. 2019 13th European Conference on Antennas and Propagation (EuCAP)*, Krakow, Poland, Mar. 2019, pp. 1–5.
- [10] H. Zhang, N. Shlezinger, F. Guidi, D. Dardari, and Y. C. Eldar, "6G wireless communications: From far-field beam steering to near-field beam focusing," *IEEE Commun. Mag.*, vol. 61, no. 4, pp. 72–77, 2023.
- [11] Z. Wang, X. Mu, and Y. Liu, "Near-field integrated sensing and communications," *IEEE Commun. Lett.*, vol. 27, no. 8, pp. 2048–2052, Aug. 2023.
- [12] Y. Zhang, X. Wu, and C. You, "Fast near-field beam training for extremely large-scale array," *IEEE Wireless Commun. Lett.*, vol. 11, no. 12, pp. 2625–2629, Dec. 2022.
- [13] Y. Liu, Z. Wang, J. Xu, C. Ouyang, X. Mu, and R. Schober, "Near-field communications: A tutorial review," *IEEE Open J. Commun. Soc.*, vol. 4, pp. 1999–2049, Aug. 2023.
- [14] E. Björnson and L. Sanguinetti, "Power scaling laws and near-field behaviors of massive MIMO and intelligent reflecting surfaces," *IEEE Open J. Commun. Soc.*, vol. 1, pp. 1306–1324, Sep. 2020.
- [15] F. Wang, X. Wang, X. Li, X. Hou, L. Chen, S. Suyama, and T. Asai, "Ring-type codebook design for reconfigurable intelligent surface near-field beamforming," in *Proc. 2022 IEEE 33rd Annual International Symposium on Personal, Indoor and Mobile Radio Communications (PIMRC)*, Kyoto, Japan, Sep. 2022, pp. 391–396.
- [16] Z. Wang, X. Mu, and Y. Liu, "Near-field integrated sensing and communications," *IEEE Commun. Lett.*, vol. 27, no. 8, pp. 2048–2052, Aug. 2023.
- [17] E. Björnson, O. T. Demir, and L. Sanguinetti, "A primer on near-field beamforming for arrays and reconfigurable intelligent surfaces," in *Proc. 2021 55th Asilomar Conference on Signals, Systems, and Computers*, Pacific Grove, CA, USA, Oct. 2021, pp. 105–112.
- [18] H. Griffiths, "From a different perspective: principles, practice and potential of bistatic radar," in *2003 Proceedings of the International Conference on Radar (IEEE Cat. No.03EX695)*, Adelaide, SA, Australia, Sep. 2003, pp. 1–7.
- [19] A. Sabharwal, P. Schniter, D. Guo, D. W. Bliss, S. Rangarajan, and R. Wichman, "In-band full-duplex wireless: Challenges and opportunities," *IEEE J. Sel. Areas Commun.*, vol. 32, no. 9, pp. 1637–1652, Sep. 2014.
- [20] M. Duarte and A. Sabharwal, "Full-duplex wireless communications using off-the-shelf radios: Feasibility and first results," in *Proc. 2010 Conference Record of the Forty Fourth Asilomar Conference on Signals, Systems and Computers*, Pacific Grove, CA, USA, 2010, pp. 1558–1562.
- [21] J. A. Zhang, F. Liu, C. Masouros, R. W. Heath, Z. Feng, L. Zheng, and A. Petropulu, "An overview of signal processing techniques for joint communication and radar sensing," *IEEE J. Sel. Topics Signal Process.*, vol. 15, no. 6, pp. 1295–1315, Nov. 2021.
- [22] C. Sturm and W. Wiesbeck, "Waveform design and signal processing aspects for fusion of wireless communications and radar sensing," *Proc. IEEE*, vol. 99, no. 7, pp. 1236–1259, July 2011.
- [23] H. L. V. Trees, *Optimum Array Processing: Part IV of Detection, Estimation, and Modulation Theory*. John Wiley & Sons, Inc., 2002.
- [24] F. Sohrabi and W. Yu, "Hybrid digital and analog beamforming design for large-scale antenna arrays," *IEEE J. Sel. Topics Signal Process.*, vol. 10, no. 3, pp. 501–513, April 2016.
- [25] *5G NR: Physical layer procedures for data*, 3GPP TS 38.214, June 2023, v17.6.0 Release 17. [Online]. Available: <https://portal.3gpp.org/desktopmodules/Specifications/SpecificationDetails.aspx?specificationId=3216>

- [26] J. Wang, Z. Lan, C. woo Pyo, T. Baykas, C. sean Sum, M. Rahman, J. Gao, R. Funada, F. Kojima, H. Harada, and S. Kato, "Beam codebook based beamforming protocol for multi-Gbps millimeter-wave WPAN systems," *IEEE J. Sel. Areas Commun.*, vol. 27, no. 8, pp. 1390–1399, Oct. 2009.
- [27] Z. Xiao, T. He, P. Xia, and X.-G. Xia, "Hierarchical codebook design for beamforming training in millimeter-wave communication," *IEEE Trans. Wireless Commun.*, vol. 15, no. 5, pp. 3380–3392, May 2016.
- [28] S. K. Dehkordi, J. C. Hauffen, P. Jung, R. Hernangomez, G. Caire, and S. Stanczak, "Multi-scatter-point target estimation for sensing-assisted OTFS automotive communication," in *WSA & SCC 2023; 26th International ITG Workshop on Smart Antennas and 13th Conference on Systems, Communications, and Coding*, Braunschweig, Germany, Feb. 2023, pp. 1–6.
- [29] W. Boyse and A. Seidl, "A hybrid finite element method for 3-D scattering using nodal and edge elements," *IEEE Transactions on Antennas and Propagation*, vol. 42, no. 10, pp. 1436–1442, Oct. 1994.
- [30] P. Kumari, J. Choi, N. González-Prelcic, and R. W. Heath, "IEEE 802.11ad-based radar: An approach to joint vehicular communication-radar system," *IEEE Trans. Veh. Technol.*, vol. 67, no. 4, pp. 3012–3027, April 2018.
- [31] D. H. N. Nguyen and R. W. Heath, "Delay and Doppler processing for multi-target detection with IEEE 802.11 OFDM signaling," in *Proc. IEEE Int. Conf. Acoustics, Speech, and Signal Processing (ICASSP)*, New Orleans, LA, USA, Mar. 2017, pp. 3414–3418.
- [32] D. C. Rife and R. R. Boorstyn, "Multiple tone parameter estimation from discrete-time observations," *Bell Syst. Tech. J.*, vol. 55, no. 9, pp. 1389–1410, Nov. 1976.
- [33] M. Kronauge and H. Rohling, "Fast two-dimensional CFAR procedure," *IEEE Trans. Aerosp. Electron. Syst.*, vol. 49, no. 3, pp. 1817–1823, 2013.
- [34] S. Blake, "OS-CFAR theory for multiple targets and nonuniform clutter," *IEEE Trans. Aerosp. Electron. Syst.*, vol. 24, no. 6, pp. 785–790, 1988.
- [35] L. Pucci, E. Matricardi, E. Paolini, W. Xu, and A. Giorgetti, "Performance analysis of a bistatic joint sensing and communication system," in *2022 IEEE International Conference on Communications Workshops (ICC Workshops)*, Seoul, Korea, Republic of, May 2022, pp. 73–78.
- [36] N. J. Willis, *Bistatic radar*, 2nd ed. SciTech Publishing, 2005.
- [37] M. Goemans and D. Williamson, "Improved approximation algorithms for maximum cut and satisfiability problems using semidefinite programming," *Journal of Association for Computing Machinery*, vol. 42, no. 6, p. 1115–1145, Nov. 1995.
- [38] P. W. Kassakian, "Convex approximation and optimization with applications in magnitude filter design and radiation pattern synthesis," PhD dissertation, University of California, Berkeley, 2006.
- [39] S. K. Dehkordi, L. Pucci, P. Jung, A. Giorgetti, E. Paolini, and G. Caire, "Multi-static parameter estimation in the near/far field beam space for integrated sensing and communication applications," 2023. [Online]. Available: <https://arxiv.org/abs/2309.14778>
- [40] V. S. Chernyak, *Fundamentals of multisite radar systems: multistatic radars and multistatic radar systems*. CRC press, 1998.
- [41] L. Scharf and C. Demeure, *Statistical Signal Processing: Detection, Estimation, and Time Series Analysis*, ser. Addison-Wesley series in electrical and computer engineering. Addison-Wesley Publishing Company, 1991.